HHS Public Access

Author manuscript

Neuroimage. Author manuscript; available in PMC 2016 June 01.

Published in final edited form as:

Neuroimage. 2015 June ; 113: 235–245. doi:10.1016/j.neuroimage.2015.03.020.

Histologic validation of locus coeruleus MRI contrast in post-mortem tissue

Noam I. Keren[a], **Saeid Taheri**[a], **Elena M. Vazey**[a], **Paul S. Morgan**[c], **Ann-Charlotte E. Granholm**[a], **Gary S. Aston-Jones**[a], and **Mark A. Eckert**[b,*]

[a]Department of Neurosciences, Medical University of SC, Charleston, SC, USA

[b]Department of Otolaryngology, Head & Neck Surgery, Medical University of SC, Charleston, SC, USA

[c]Medical Physics, Nottingham University Hospitals, NHS Trust, Nottingham, UK

Abstract

The locus coeruleus (LC) noradrenergic system regulates arousal and modulates attention through its extensive projections across the brain. LC dysfunction has been implicated in a broad range of neurodevelopmental, neurodegenerative and psychiatric disorders, as well as in the cognitive changes observed during normal aging. Magnetic resonance imaging (MRI) has been used to characterize the human LC (elevated contrast relative to surrounding structures), but there is limited understanding of the factors underlying putative LC contrast that are critical to successful biomarker development and confidence in localizing nucleus LC. We used ultra-high-field 7 T magnetic resonance imaging (MRI) to acquire T1-weighted microscopy resolution images (78 μm in-plane resolution) of the LC from post-mortem tissue samples. Histological analyses were performed to characterize the distribution of tyrosine hydroxylase (TH) and neuromelanin in the scanned tissue, which allowed for direct comparison with MR microscopy images. Our results indicate that LC-MRI contrast corresponds to the location of neuromelanin cells in LC; these also correspond to norepinephrine neurons. Thus, neuromelanin appears to serve as a natural contrast agent for nucleus LC that can be used to localize nucleus LC and may have the potential to characterize neurodegenerative disease.

Keywords

Neuromelanin; Post-mortem; Histology; MRI; Brainstem; Norepinephrine; Inversion recovery

Introduction

The nucleus locus coeruleus (LC) modulates arousal (Aston-Jones et al., 1984; Jouvet, 1969; Vazey and Aston-Jones, 2014) and attentional states (Aston-Jones et al., 2000; Aston-Jones and Cohen, 2005; Carli et al., 1983) through its extensive noradrenergic connections with cortical and sub-cortical brain regions (Morrison et al., 1982; Porrino and Goldman-Rakic,

*Corresponding author at: MSC 550, Department of Otolaryngology, Head and Neck Surgery, Medical University of South Carolina, Charleston, SC 29425, USA., eckert@musc.edu (M.A. Eckert).

1982; Morrison and Foote, 1986; Morecraft et al., 1992). Atypical development or degeneration of LC has been implicated in the etiology of a variety of disorders involving cognitive dysfunction, including Down syndrome, Parkinson's disease, and Alzheimer's disease (Mann and Yates, 1983; Chan-Palay and Asan, 1989a; Chan-Palay, 1991; German et al., 1992; Braak et al., 2000; Zarow et al., 2003; Vazey and Aston-Jones, 2012). A biomarker of LC structural integrity would aid in the characterization of LC etiology in these and other disorders, and could guide targeted pharmacotherapies for individuals with LC dysfunction.

Magnetic resonance imaging (MRI) has been used to identify putative LC structural contrast, or elevated signal relative to surrounding tissue, using a T1-weighted turbo spin echo (T1-TSE) sequence with clinical 3 T MR scanners (Sasaki et al., 2006; Keren et al., 2009). This contrast or hyperintensity is typically visible in the dorsal pons at the level of the trochlear nucleus where LC noradrenergic neurons are particularly dense (German et al., 1988; Chan-Palay and Asan, 1989b; Manaye et al., 1995). The histologic basis for putative LC contrast in the T1-TSE MRI scan is unclear, but necessary for understanding the extent to which MRI contrast can be used as a biomarker for neurodegenerative diseases that exhibit nucleus LC decline (Ohtsuka et al., 2013).

One explanation for LC contrast in MRI scans is that neuromelanin pigment contributes to the contrast because a similar hyperintensity is observable in the substantia nigra with T1-TSE MRI scans where neuromelanin also accumulates (Sasaki et al., 2006). Neuromelanin is a byproduct of neuronal norepinephrine (NE) and dopamine synthesis, accumulating in cell bodies beginning in early childhood and increasing in concentration throughout life (Zecca et al., 2004; Halliday et al., 2006). Thus, neuromelanin is a target for biomarker development to characterize neurodegenerative diseases where low contrast is predicted to occur with LC neuron loss in older adult samples. This hypothesis is supported by human post-mortem 3 T MRI imaging of the substantia nigra in which neuromelanin contributes to T1-TSE contrast (Kitao et al., 2013).

We tested the hypothesis that LC contrast seen in TSE sequences can be attributed to neuromelanin that accumulates in nucleus LC. Ultra-high field 7 T imaging was used to demonstrate consistent putative LC-MRI contrast using human post-mortem brainstems. Histology was performed to show that neuromelanin and tyrosine hydroxylase (TH) containing LC neurons corresponded to the presence of LC-MRI contrast for this histological case study that leveraged the spatially varying location of LC-MRI contrast and density of neuromelanin and TH in the left and right LC. Thus, ultra-high field imaging was used to obtain sufficient resolution for integration with histologic data to provide cellular-level evidence for the basis of LC-MRI contrast.

Materials and methods

Brainstem samples and tissue preparation

Post-mortem brainstem samples from the Medical University of South Carolina Carroll A. Campbell, Jr. Neuropathology Laboratory were used to establish imaging methods that consistently demonstrated LC-MRI contrast. These samples included tissue from

approximately the superior colliculus level rostrally to the obex caudally. The brainstems were from 4 females and 3 males with an age range of 62–91 years, and a donor mean age of 76.4 years (standard deviation, *SD* = 9.5; see Table 1). The mean post-mortem interval between death and tissue extraction at autopsy was 9.11 h (*SD* = 7.18) and mean delay from extraction to fixation was 2.14 h (*SD* = 1.95). All the samples were obtained from donors whose next of kin provided a postmortem consent for tissue donation as approved by the Medical University of South Carolina Institutional Review Board and in accordance with the Declaration of Helsinki. The donor identity was kept anonymous from the arrival of the tissue to the laboratory and a random identifier was assigned to each donor that could not be linked to personal data for the donor.

The brainstem samples were selected to ensure intact anatomical structures throughout the rostro-caudal extent of the 4th ventricle and complete pons. Exclusion criteria for brainstem tissue selection included any gross pathological alterations observed in the pons or cerebellum. The brainstem was separated from the rest of the brain via scalpel separation at the level of the superior colliculus dorsally and rostral to the substantia nigra ventrally. The brainstem specimens were fixed in 4% paraformaldehyde solution for an average of 72 h and then transferred to 30% sucrose in 0.1 M phosphate buffer (PB) solution for 7–10 days and stored in cryoprotectant at −20 °C. The clinical history of each donor and tissue pathology was established using clinical records and postmortem examination by a licensed neurologist and neuropathologist according to the National Institutes on Aging (NIA) criteria for AD staging (Jack et al., 2012). Six of the 7 subjects had received a neuropathological diagnosis of AD, and the last subject was found to have neuropathological features consistent with LBD (Table 1). Again, these data were used to establish imaging methods and there were too few cases to perform individual difference analyses.

All accessible brainstem arterial branches and vessels were carefully removed to prevent susceptibility artifacts from intravascular (blood) iron. To maintain morphology and avoid tissue distortion (Smith et al., 1994; Benveniste and Blackband, 2002), brainstems were embedded in sterile 4% agar–saline in a 120 ml MRI compatible container (Fisher Scientific) and stored at 4 °C before MRI scanning. To prevent differences in image contrast caused by temperature variations (Bloembergen et al., 1948; De Poorter, 1995; Chen et al., 2006), all specimens were allowed to reach room temperature (25 °C) before imaging. Sample temperature was verified immediately before image acquisition (*M* = 25.45 °C, *SD* = 0.35). Samples were centered inside the scanner and protected from vibration in a custom MRI-compatible foam cradle.

Magnetic resonance imaging

All MRI scans were collected using a BioSpec 70/30 USR 7 T system at the MUSC Center for Biomedical Imaging. The scanner was equipped with a 72 mm 1H quadrature volume transmitter–receiver coil and operated with ParaVision 5.0 operating software (Bruker BioSpin MRI GmbH, Germany). To obtain optimal LC-related contrast we acquired images with the following parameters: echo time (TE; 9.8, 12.3, 14.8, 17.3, 19.8, 24.8, 29.8, 34.8, and 39.8 ms) and inversion time (TI; 325, 825 and 1325 ms). Each variable was manipulated separately, and a low resolution was utilized to leverage scanning time while maintaining

sufficient LC-associated contrast. Common RARE-INV sequence parameters across the acquisitions to optimize contrast were: number of slices = 8, slice thickness = 2 mm, slice spacing = 0.5 mm, repetition time (TR) = 3000 msec, number of averages = 3, imaging resonance frequency = 300 MHz, echo train length = 2, flip angle = 180°, matrix size = 128 × 128, field of view (FOV) = 4.00 × 4.00 cm, and in-plane voxel size = 310 μm.

For comparison of putative LC-MRI contrast with cytological spatial distribution in the same tissue, we aimed to acquire scans at microscopy (<100 μm) in-plane resolution (Johnson et al., 1993; Benveniste and Blackband, 2002). For each ex-vivo sample we first acquired a reference scan that was used to align the RARE-INV scan volume geometry. In particular, the volume bounding box was placed to encompass the entire tissue sample and oriented to ensure that axial slices are perpendicular to the rostral–caudal axis of the brainstem. The following sequence parameters were used to obtain microscopy resolution images of the LC in postmortem tissue: number of slices = 18, slice thickness = 2 mm, slice spacing = 0.5 mm, TR = 3000 ms, TE = 14.8 ms, TI = 825 ms, number of averages = 5, imaging resonance frequency = 300 MHz, echo train length = 2, flip angle = 180°, matrix size = 512 × 512, FOV = 4.00 × 4.00 cm, and in-plane voxel size = 78 μm. Images were reconstructed at 16-bit dynamic range resolution (65,535 values). The total scan time for each brainstem volume was 3 h 11 min.

Histology

Tissue selection and preparation—A case study design was used so that we could provide detailed descriptions of the histologic features that co-occur with LC-MRI contrast. This type of design is useful for characterizing histologic substrates of MRI contrast (Bolding et al., 2013; Kitao et al., 2013). Our approach was designed to provide detailed evidence of histologic features underlying LC-MRI contrast that can be targeted in larger scale studies. Moreover, we leveraged the spatial distribution variation of LC-MRI contrast within and across brainstem sections to better specify histologic properties that produce LC-MRI contrast.

The histological analyses in this study were performed on a brainstem sample that exhibited a substantial difference in left and right putative LC-MRI contrast (female, 91 years of age). A 15 mm block of the pons that covered the extent of the image acquisition was incubated in 0.1 M PB with 30% sucrose in for 72 h prior to cryosectioning. The tissue was flash frozen in liquid nitrogen and fully embedded in OCT mounting medium with the 4th ventricle structure intact. The mounted tissue block was equilibrated to −20 °C before sectioning at 40 μm-thickness on a HM 500 cryostat (Microm GmbH, Walldorf, Germany). Free floating sections were collected in 0.1 M PB with 0.1% sodium azide at 4 °C, in consecutive wells in a 24-well plate, so that sequential sections in each well/series were 400 μm apart.

Hematoxylin & eosin (H&E) staining—A modified Mayer's hematoxylin & eosin (H&E) procedure (Allen, 1992) was used to visualize anatomical features and facilitate the detection of nucleus LC adjacent to the periaqueductal gray region. Sections were mounted on cleaned glass microscope slides, dried and defatted in xylene (2 × 10 min; Fisher Scientific), rehydrated in alcohol (ethyl alcohol: 100%, 10 min; 95%, 5 min; 70%, 3 min;

50%, 3 min), and distilled water (3 min) before staining in hematoxylin (H3136; Sigma-Aldrich, Saint Louis, MO, USA) for 5 min. The slides were washed in running tap water for 20 s before being counter-stained in eosin Y (E4382; Sigma-Aldrich) and phloxine B (4030; Sigma-Aldrich) solution for 2 min. Slides were then dehydrated (ethyl alcohol: 95%, 4 min; 100%, 5 min), cleared in xylene (10 min) and cover-slipped with DPX mounting media (SPI5-100; Fisher Scientific, Fair Lawn, NJ, USA).

Tyrosine hydroxylase immunohistochemistry—Free-floating immunohistochemistry for tyrosine hydroxylase (TH) was used to visualize norepinephrine cells in LC from a parallel series of sections. Sections were blocked in 10% goat serum in Tris-buffered saline with Tween-20 (TBS-T) solution for 1 h and incubated with rabbit anti-TH primary antibody (1:1000; P40101; Pel-Freez Biologicals, Rogers, AR, USA) diluted in 3% goat serum TBS-T for 48 h at 4 °C. Sections were then incubated with a biotinylated goat anti-rabbit antibody (1:200; BA-1000; Vector Laboratories, Burlingame, CA, USA) with 3% goat serum in TBS for 1 h, and then in Vectastain ABC 1:500 in TBS-T (SK-4005) for 1 h. Staining was visualized with Vector VIP peroxidase for 10 min (SK-4600; Vector Laboratories). The sections were mounted on glass slides, dried, dehydrated in alcohol, defatted in xylene and cover slipped using DPX mounting media.

Neuromelanin histology—An unstained series of LC sections was mounted onto glass slides, dehydrated, defatted and cover slipped with DPX mounting media for quantification of pigmented neuromelanin (Fedorow et al., 2006). Tissue sections from three representative rostral–caudal locations of the pons corresponding to the 2 mm MR slices were selected to visualize neuromelanin distribution in the nucleus LC. Neuromelanin appeared as a brown pigmented structure in the unstained sections.

Microscopy—High-resolution virtual slices with manual focus correction were acquired from the unstained (neuromelanin) and stained (TH, H&E) sections using 10× and 2× objectives, respectively, of a Nikon Eclipse E600 (Nikon, Japan) with a CCD camera and Stereo Investigator software (v9.13, MicroBrightField, Inc., Williston, VT, USA). The same light settings, exposure and white-balance parameters were used in all imaging. Authors EMV and GSAJ examined and confirmed qualitative descriptions of the histological data.

Image pre-processing—Density maps from TH-stained sections across the space of the MRI slices were obtained by converting the histologic images to binary 8 bit images with an inverted lookup table and down-sampling the images to 512 × 512 pixels to match the matrix size of the MRI acquisition. The binary histologic images were then co-registered and summed across 5 slices within the axial anatomical space corresponding to the thickness of each MRI slice (2 mm) to create a TH density map to characterize the consistency of TH-stained cells across the space of the corresponding MRI slice. Thus, the density map was a sum of the binary representations of TH across the slices corresponding to the section thickness of the MRI data. All MRI scans were realigned on the axial, sagittal and coronal planes for visualization using SPM8 (Wellcome Department of Cognitive Neurology, University College, London, UK; http://www.fil.ion.ucl.ac.uk/spm/). To facilitate co-registration of histological and MR images, an anatomical reference origin was set at the

anterior medullary vellum. The SPM8 Check Registration tool was then used to manually rigidly align the histological and MRI images.

Results

MR imaging methods for imaging LC

The ex-vivo LC imaging protocol was optimized for high resolution histological comparisons and enhanced LC-associated MRI contrast. Fig. 1 demonstrates the effects of different acquisition parameters on putative MR contrast in LC and surrounding tissue. The sequences required adjustment to account for (1) the increase in magnetic field strength (i.e., 3 T vs. 7 T MRI system) and associated T1 time lengthening with convergence of longitudinal relaxation, which can limit tissue contrast (Benveniste and Blackband, 2002); and (2) the impact of aldehyde-based post-mortem tissue fixation that creates molecular binding and proton micro-environment changes in fixative penetrated tissue (Tovi and Ericsson, 1992; Pfefferbaum et al., 2004; Shepherd et al., 2009).

Ex-vivo imaging of fixed tissue resulted in less contrast between LC and the periaqueductal gray (PAG; Fig. 1) than we previously obtained with 3 T in vivo imaging using a similar T1-TSE sequence (Keren et al., 2009). The RARE sequence was therefore modified to include a longer repetition time and inversion recovery (RARE-INV), in addition to changes in echo times, to optimize a sequence for characterizing putative LC contrast from that of the PAG and other adjacent structures. Longer time to inversion increased LC contrast (Fig. 1A vs. 1B), whereas intensity from surrounding tissue was minimized by shorter echo times (Figs. 1C–E).

The final protocol provided an in-plane resolution of 78 μm compared to a typical in vivo 3 T acquisition with a resolution of 500 μm (Figs. 2A,B). Comparison of the RARE-INV microscopy image with a traditional H&E microscopy image from the same tissue demonstrates that our sequence allows comparison of gross cellular field morphology between MR and traditional histological techniques (Figs. 2B, C).

Elevated bilateral contrast was consistently observed at the level of the dorsal pons in the RARE-INV images (Fig. 3). These bilateral hyperintensities were located at the corner of the 4th ventricle, at the approximate location of nucleus LC, and adjacent to the hypointensities of the putative medial longitudinal fasciculus and superior cerebellar peduncle. Hyperintensities could also be seen in the substantia nigra region (Fig. 4). Thus, the RARE-INV microscopy acquisition produced a similar pattern of hyperintensities in the putative LC and substantia nigra contrast as reported previously in in vivo studies using a T1-TSE sequence at 3 T (Sasaki et al., 2006; Keren et al., 2009), although with a substantial increase in spatial resolution of anatomical features that is demonstrated in Fig. 2.

White matter tracts were not observable in all samples (e.g., medial longitudinal fasciculus in HB13, Fig. 3). In addition, there was variation between the LC contrast and surrounding tissue across samples. Moreover, RARE-INV MR microscopy identified clear hemispheric differences in putative LC contrast within samples (Figs. 3, 4). Note the hemispheric asymmetry in size and shape of the putative LC contrast through slices 5–7 in Fig. 4.

Histological validation with TH density mapping

To validate the anatomical detail and potential substrates underlying LC contrast in our MR microscopy sequence, we undertook histological analyses on one sample (HB24; Figs. 3, 4) that exhibited a particularly asymmetric LC morphology (Table 1). This approach allowed us to explore the impact of within-subject differences in TH and neuromelanin deposition on putative LC-MRI contrast, with limited confounds from fixation differences across samples (Table 1).

TH density maps were created from summing across 5 serial TH-stained sections anatomically corresponding to each 2 mm-thick MRI slice. These maps provided detailed information on the location and density of TH+ neurons and processes potentially contributing to LC-MRI contrast in these regions. The impact of relatively thick MRI slices and the importance of summing across the histologic sections is demonstrated in Fig. 5 where MRI contrast is elevated in the right LC where there is consistent TH staining across sections, in contrast to the left LC results where TH is inconsistently evident across histological sections and exhibits limited LC-MRI contrast.

Fig. 6 further demonstrates that TH density was critical for observing LC-MRI contrast across brainstem slices. Hemispheric asymmetry in TH histology corresponded to the hemispheric asymmetry in contrast across the MRI slices of the same region (Figs. 5 and 6 slices 5–7). In particular, the rostral right side of the sample exhibited relatively weak LC-MRI contrast (Fig. 6: slice 5) where there were sparse TH+ cell bodies with limited neurite processes. The rostral left side of the sample exhibited stronger LC-MRI contrast and increased TH positive neurons and processes compared to the right side (slice 5). LC-MRI contrast was relatively pronounced bilaterally in slice 6 where this sample exhibited the highest density of TH+ cells. Thus, LC-MRI contrast does not occur unless there is TH in the same anatomical space.

Histologic specificity of LC-MRI contrast

The TH density maps provided gross morphologic evidence for where LC-MRI contrast should be most pronounced. There were regions, however, where TH was present in the absence of elevated MRI contrast. For example, Fig. 7 shows that elevated MRI contrast was not observed in the caudal dorsal raphe nucleus that contains numerous TH+ neurons (Baker et al., 1991). Importantly, neuromelanin does not accumulate in the dorsal raphe (Fig. 7). Similarly, elevated contrast was not observed in TH+ LC neurites (Figs. 5 & 8) where there was no neuromelanin.

To emphasize the observation that LC-MRI contrast occurs with the presence of neuromelanin in TH positive cell bodies, Fig. 8 shows that the spatial distribution of LC-MRI contrast was consistent with the spatial distribution of neuromelanin in the LC region. Ellipsoid-shaped distributions of neuromelanin and LC-MRI contrast were present on the left compared to oval distributions of neuromelanin and LC-MRI contrast on the right. Thus, LC-MRI contrast is most pronounced in the presence of dense neuromelanin clusters and TH-positive neurons.

In summary, the results demonstrate neuromelanin as a primary source of LC-MRI contrast based on: 1) the presence of LC-MRI contrast with neuromelanin containing TH+ LC cell bodies; 2) the corresponding asymmetrical and shape pattern of LC-MRI and neuromelanin; and 3) the absence of LC-MRI contrast in the raphe nucleus where TH+ cell bodies were observed without neuromelanin, and in the TH+ LC processes where neuromelanin was not observed.

Discussion

We have demonstrated here that LC-MRI contrast in human postmortem tissue spatially overlaps with the cellular field of nucleus LC and is dependent on the presence of neuromelanin. There was a strong correspondence between the distribution of contrast in the high-resolution images (78 μm in-plane voxel size) and the distribution of neuromelanin in histological sections, as well as the distribution of TH-containing neurons. Thus, the LC-MRI contrast obtained here provides a marker of the NE-producing neurons in nucleus LC.

The overarching goal of this study was to examine the histologic basis for LC-MRI contrast in the LC region in order to better understand the meaning of LC-MRI contrast as a marker for localizing LC in neuroimaging experiments (Keren et al., 2009) and as an in vivo biomarker for LC degeneration (Matsuura et al., 2013; Ohtsuka et al., 2013; Takahashi et al., in press). An in vivo biomarker for LC degeneration would be useful for clinical diagnosis because LC degeneration corresponds with several disorders, e.g., the severity of subsequent Parkinson's disease (PD) symptoms (Buchman et al., 2012), and with cognitive decline associated with age (Wilson et al, 2013). Our results indicate that in vivo LC contrast does indicate the location of LC neurons containing neuromelanin and needs to be evaluated in the context of the accumulation of neuromelanin.

Our study included tissue from people with a history of AD or LBD, which are both characterized by a loss of LC neurons (Chan-Palay and Asan, 1989a; German et al., 1992; Zarow et al., 2003; Grudzien et al., 2007). Interestingly, there was marked variance in the shape or distribution of LC-MRI contrast across samples (e.g., Fig. 3). Although our histological case study focused on tissue from a donor who had a neuropathological diagnosis of AD and therefore may not be representative of the older adult population, selection of this tissue was advantageous because it exhibited spatially varying LC morphology across the brainstem. This within case analysis is a valuable approach because fixation times can vary across cases. Thus, each section and side of the brainstem served as a source of cytoarchitectural variance for a sample that had a short post-mortem interval to fixation. The figures show that the spatially varying density of TH and the presence of neuromelanin strongly correspond to the location of LC-MRI contrast, thereby explaining why LC-MRI contrast can be present.

Individual differences are an important consideration for studies involving neuromelanin and LC-MRI, including for our histological results from a 91 year old donor. Neuromelanin accumulates in cells throughout life, with the greatest concentration of neuromelanin observed in the second half of life (Zucca et al., 2006). Shibata et al. (2006) reported a non-linear association between LC-MRI contrast and age that was generally consistent with a

non-linear association between age and neuromelanin concentration (Zecca et al., 2004). In addition, the position of maximal LC-MRI contrast was more likely to be increasingly caudal with increasing age (Keren et al., 2009), consistent with a greater rostral loss of LC neurons with age (Manaye et al., 1995). There were too few tissue samples (n = 7) in our study to perform correlational analyses, but there was a wide range of LC-MRI contrast within and across samples that appeared unrelated to age. Cognitive data were not available for our samples, but the high variability in LC-MRI contrast indicates that future studies could characterize the extent to which LC-MRI contrast predicts the early executive function symptoms in people with pre-clinical Alzheimer's or Parkinson's disease (Saunders and Summers, 2011; Salmon, 2012; Rochat et al., 2013), and the extent to which LC-MRI can serve as a biomarker for such disorders (Hampel et al., 2010).

Our methods were optimized to obtain high spatial resolution images (78 μm in plane) in comparison to the standard ~500 μm in-plane resolution that is typically used to image LC in human subjects. Fig. 2 shows how noisy these ~500 μm data can be in comparison to our 78 μm data because of physiological motion, lower field strength, and shorter scanning time. Thus, future studies linking LC histology to LC-MRI contrast at 3 T will be important for evaluating an LC-MRI biomarker.

A limitation of previous in vivo studies on LC-MRI, and the current study, is that the MRI data is T1-weighted and not quantitative. Semi-quantitative methods (e.g., using contrast from adjacent tissue as a baseline control) are necessary to obtain values for group comparisons using T1-weighted data (Matsuura et al., 2013; Ohtsuka et al., 2013). A concern for this approach is that tissue serving as the baseline measurement might be atypical in neurodegenerative diseases. Quantitative imaging methods are necessary to avoid these confounds, and would be critical for implementation of an imaging biomarker.

One explanation for the LC contrast mechanism in multi-slice T1-TSE acquisitions is off-resonance magnetization transfer effects that have been observed for multi-slice acquisitions (Dixon et al. 1990). In support of this explanation, a gradient echo magnetization transfer sequence was developed to image LC (Nakane et al., 2008) and this sequence appears to provide greater LC contrast to noise than a T1-TSE sequence (Chen et al., 2014). Thus, magnetization transfer ratio may be useful in quantifying neuromelanin in LC, but the extant literature is not clear about the degree to which LC contrast is also present when the off-resonance preparation is not applied.

The development of quantitative imaging methods for LC is challenging in human subjects because of physiological noise and motion relative to the small size of LC. Our ex vivo results indicate that imaging of melanin-like particles may be useful in developing a quantitative sequence. For example, Ju et al. (2013) examined synthetic melanin particles and found elevated T1 contrast for melanin compared to water, but only when ferritin was included with the melanin. A proposed function of neuromelanin is to collect free metals, such as iron, copper and manganese that could damage a cell (Zecca et al., 2006). These metals are bound to neuromelanin in LC and could therefore contribute to the LC-MRI contrast that we observed. However, Kitao et al. (2013) included a ferritin stain in their study of the substantia nigra using a T1-weighted sequence and did not observe a

relationship between substantia nigra MRI contrast and ferritin density. Although LC neuromelanin may have more manganese and copper than iron (Zecca et al., 2004), the similarity of our substantia nigra hyperintensity observation with that in the Kitao et al. (2013) study, as well as the different concentrations of metals across melanin-containing nuclei, suggest that neuromelanin itself is the primary contributor to LC-MRI contrast. This conclusion is supported by our observation that TH neurons in LC (which contain relatively high levels of neuromelanin compared to other monoaminergic neurons) produce strong MRI contrast whereas similar TH neurons in dorsal raphe (lacking neuromelanin in histological stains) did not (Fig. 7). This interpretation is strengthened by evidence that melanin-containing tumors produce T1 shortening (Frieden et al., 1994; Premkumar et al., 1996; Koral et al., 2010). The magnetic interaction between neuromelanin and the surrounding tissue environment, as well as the degree to which neuromelanin is membrane-bound, are likely key factors in the generation of the associated T1 contrast.

Conclusion

We have demonstrated that neuromelanin is a primary contributor to LC-MRI contrast that is observed in neuroimaging studies of human subjects. In particular, hemispheric asymmetry in neuromelanin corresponded to asymmetric LC-MRI contrast. Moreover, the ultra-high resolution in our analyses provided evidence that the distribution of TH and neuromelanin corresponded to the shape and distribution of LC-MRI contrast. These results indicate that neuromelanin serves as a natural contrast agent for identifying the location of nucleus LC. Further development of a sensitive and quantitative sequence in normative and neurodegenerative disease samples will help establish LC-MRI contrast as a clinically feasible method to aid in clinical decision making for people with neurodegenerative disease that involves LC, but the low resolution of 3 T data and physiological noise at higher fields are challenges that must be addressed to obtain a reliable metric of LC neuromelanin.

Acknowledgments

We thank the Medical University of South Carolina Carroll A. Campbell, Jr. Neuropathology Laboratory, and Nicholas Gregory, Cindy Welsh, and Laura Columbo for their assistance with this research. This work was supported by PHS grants R01-MH092868 and R21-MH099534, and by the MUSC Center for Biomedical Imaging and the Charles and Dianne Barmore Fund for Parkinson's Research.

References

Allen, TC. Hematoxylin and eosin. In: Prohpet, EB.; Mills, B.; Arrington, JB.; Sobin, LH., editors. Laboratory Methods in Histotechnology. 1. American Registry of Pathology; Washington, DC: 1992. p. 53-58.

Aston-Jones G, Cohen JD. Adaptive gain and the role of the locus coeruleusnorepinephrine system in optimal performance. J Comp Neurol. 2005; 493:99–110. [PubMed: 16254995]

Aston-Jones, G.; Foote, SL.; Bloom, F. Anatomy and physiology of locus coeruleus neurons: functional implications. In: Ziegler; Lake, CR., editors. Norepinephrine (Frontiers of Clinical Neuroscience). Vol. 2. Williams and Wilkins Co; Baltimore: 1984. p. 92-116.

Aston-Jones G, Rajkowski J, Cohen J. Locus coeruleus and regulation of behavioral flexibility and attention. Prog Brain Res. 2000; 126:165–182. [PubMed: 11105646]

Baker KG, Halliday GM, Hornung JP, Geffen LB, Cotton RG, Törk I. Distribution, morphology and number of monoamine-synthesizing and substance P-containing neurons in the human dorsal raphe nucleus. Neuroscience. 1991; 42(3):757–775. [PubMed: 1720227]

Benveniste H, Blackband S. MR microscopy and high resolution small animal MRI: applications in neuroscience research. Prog Neurobiol. 2002; 67:393–420. [PubMed: 12234501]

Bloembergen N, Purcell E, Pound R. Relaxation effects in nuclear magnetic resonance absorption. Phys Rev. 1948; 73:679–712.

Bolding MS, Reid MA, Avsar KB, Roberts RC, Gamlin PD, Gawne TJ, White DM, den Hollander JA, Lahti AC. Magnetic transfer contrast accurately localizes substantia nigra confirmed by histology. Biol psychiatry. 2013; 73(3):289–294. [PubMed: 22981657]

Braak H, Rüb U, Sandmann-Keil D, Gai WP, de Vos RAI, Jansen Steur ENH, Arai K, Braak E. Parkinson's disease: affection of brain stem nuclei controlling premotor and motor neurons of the somatomotor system. Acta Neuropathol. 2000; 99:489–495. [PubMed: 10805091]

Buchman AS, Nag S, Shulman JM, Lim AS, VanderHorst VG, Leurgans SE, Schneider JA, Bennett DA. Locus coeruleus neuron density and parkinsonism in older adults without Parkinson's disease. Mov Disord. 2012; 27(13):1625–1631. [PubMed: 23038629]

Carli M, Robbins TW, Evenden JL, Everitt BJ. Effects of lesions to ascending noradrenergic neurones on performance of a 5-choice serial reaction task in rats; implications for theories of dorsal noradrenergic bundle function based on selective attention and arousal. Behav Brain Res. 1983; 9(3):361–380. [PubMed: 6639741]

Chan-Palay V. Alterations in the locus coeruleus in dementias of Alzheimer's and Parkinson's disease. Prog Brain Res. 1991; 88:625–630. [PubMed: 1726030]

Chan-Palay V, Asan E. Alterations in catecholamine neurons of the locus coeruleus in senile dementia of the Alzheimer type and in Parkinson's disease with and without dementia and depression. J Comp Neurol. 1989a; 287:373–392. [PubMed: 2570794]

Chan-Palay V, Asan E. Quantitation of catecholamine neurons in the locus coeruleus in human brains of normal young and older adults and in depression. J Comp Neurol. 1989b; 287:357–372. [PubMed: 2570793]

Chen J, Daniel BL, Pauly KB. Investigation of proton density for measuring tissue temperature. J Magn Reson Imaging. 2006; 23:430–434. [PubMed: 16463298]

Chen X, Huddleston DE, Langley J, Ahn S, Barnum CJ, Factor SA, Levey AI, Hu X. Simultaneous imaging of locus coeruleus and substantia nigra with a quantitative neuromelanin MRI approach. Magn Reson Imaging. 2014; 32:1301–1306. [PubMed: 25086330]

De Poorter J. Noninvasive MRI thermometry with the proton resonance frequency method: study of susceptibility effects. Magn Reson Med. 1995; 34:359–367. [PubMed: 7500875]

Dixon WT, Engels H, Castillo M, Sardashti M. Incidental magnetization transfer contrast in standard multislice imaging. Magn reson imaging. 1990; 8(4):417–422. [PubMed: 2392030]

Fedorow H, Halliday GM, Rickert CH, Gerlach M, Riederer P, Double KL. Evidence for specific phases in the development of human neuromelanin. Neurobiol Aging. 2006; 27(3):506–512. [PubMed: 15916835]

Frieden IJ, Williams ML, Barkovich AJ. Giant congenital melanocytic nevi: brain magnetic resonance findings in neurologically asymptomatic children. J Am Acad Dermatol. 1994; 31:423–429. [PubMed: 8077466]

German DC, Walker BS, Manaye K, Smith WK, Woodward DJ, North AJ. The human locus coeruleus: computer reconstruction of cellular distribution. J Neurosci. 1988; 8:1776–1788. [PubMed: 3367220]

German DC, Manaye KF, White CL, Woodward DJ, McIntire DD, Smith WK, Kalaria RN, Mann DM. Disease-specific patterns of locus coeruleus cell loss. Ann Neurol. 1992; 32:667–676. [PubMed: 1449247]

Grudzien A, Shaw P, Weintraub S, Bigio E, Mash DC, Mesulam MM. Locus coeruleus neurofibrillary degeneration in aging, mild cognitive impairment and early Alzheimer's disease. Neurobiol Aging. 2007; 28:327–335. [PubMed: 16574280]

Halliday GM, Fedorow H, Rickert CH, Gerlach M, Riederer P, Double KL. Evidence for specific phases in the development of human neuromelanin. J Neural Transm. 2006; 113:721–728. [PubMed: 16604299]

Hampel H, Frank R, Broich K, Teipel SJ, Katz RG, Hardy J, Herholz K, Bokde AL, Jessen F, Hoessler YC, Sanhai WR, Zetterberg H, Woodcock J, Blennow K. Biomarkers for Alzheimer's disease:

academic, industry and regulatory perspectives. Nat Rev Drug Discov. 2010; 9(7):560–574. [PubMed: 20592748]

Jack CR Jr, Knopman DS, Weigand SD, Wiste HJ, Vemuri P, Lowe V, Kantarci K, Gunter JL, Senjem ML, Ivnik RJ, Roberts RO, Rocca WA, Boeve BF, Petersen RC. An operational approach to National Institute on Aging-Alzheimer's Association criteria for preclinical Alzheimer disease. Ann Neurol. 2012; 71(6):765–775. [PubMed: 22488240]

Johnson GA, Benveniste H, Black RD, Hedlund LW, Maronpot RR, Smith BR. Histology by magnetic resonance microscopy. Magn Reson Q. 1993; 9:1–30. [PubMed: 8512830]

Jouvet M. Biogenic amines and the states of sleep. Science. 1969; 163(3862):32–41. [PubMed: 4303225]

Ju KY, Lee JW, Im GH, Lee S, Pyo J, Park SB, Lee JH, Lee JK. Bio-inspired, melanin-like nanoparticles as a highly efficient contrast agent for T1-weighted magnetic resonance imaging. Biomacromolecules. 2013; 14:3491–3497. [PubMed: 23987128]

Keren NI, Lozar CT, Harris KC, Morgan PS, Eckert MA. In vivo mapping of the human locus coeruleus. NeuroImage. 2009; 47:1261–1267. [PubMed: 19524044]

Kitao S, Matsusue E, Fujii S, Miyoshi F, Kaminou T, Kato S, Ito H, Ogawa T. Correlation between pathology and neuromelanin MR imaging in Parkinson's disease and dementia with Lewy bodies. Neuroradiology. 2013; 55(8):947–953. [PubMed: 23673875]

Koral K, Derinkuyu B, Timmons C, Schwartz-Dabney CL, Swift D. Melanotic neuroectodermal tumor of infancy: report of one calvarial lesion with T1 shortening and one maxillary lesion. Clin Imaging. 2010; 34:382–384. [PubMed: 20813304]

Manaye KF, McIntire DD, Mann DM, German DC. Locus coeruleus cell loss in the aging human brain: a non-random process. J Comp Neurol. 1995; 358:79–87. [PubMed: 7560278]

Mann D, Yates P. Possible role of neuromelanin in the pathogenesis of Parkinson's disease. Mech Ageing Dev. 1983; 21:193–203. [PubMed: 6865505]

Matsuura K, Maeda M, Yata K, Ichiba Y, Yamaguchi T, Kanamaru K, Tomimoto H. Neuromelanin magnetic resonance imaging in Parkinson's disease and multiple system atrophy. Eur Neurol. 2013; 70:70–77. [PubMed: 23796701]

Morecraft RJ, Geula C, Mesulam MM. Cytoarchitecture and neural afferents of orbitofrontal cortex in the brain of the monkey. J Comp Neurol. 1992; 323:341–358. [PubMed: 1460107]

Morrison JH, Foote SL. Noradrenergic and serotoninergic innervation of cortical, thalamic, and tectal visual structures in Old and New World monkeys. J Comp Neurol. 1986; 243:117–138. [PubMed: 3950077]

Morrison JH, Foote SL, O'Connor D, Bloom FE. Laminar, tangential and regional organization of the noradrenergic innervation of monkey cortex: dopamine-beta-hydroxylase immunohistochemistry. Brain Res Bull. 1982; 9:309–319. [PubMed: 6756551]

Nakane T, Nihashi T, Kawai H, Naganawa S. Visualization of neuromelanin in the substantia nigra and locus ceruleus at 1.5 T using a 3D-gradient echo sequence with magnetization transfer contrast. Magn Reson Med. 2008; 7(4):205–210.

Ohtsuka C, Sasaki M, Konno K, Koide M, Kato K, Takahashi J, Takahashi S, Kudo K, Yamashita F, Terayama Y. Changes in substantia nigra and locus coeruleus in patients with early-stage Parkinson's disease using neuromelanin-sensitive MR imaging. Neurosci Lett. 2013; 541:93–98. [PubMed: 23428505]

Pfefferbaum A, Sullivan EV, Adalsteinsson E, Garrick T, Harper C. Postmortem MR imaging of formalin-fixed human brain. NeuroImage. 2004; 21:1585–1595. [PubMed: 15050582]

Porrino LJ, Goldman-Rakic PS. Brainstem innervation of prefrontal and anterior cingulate cortex in the rhesus monkey revealed by retrograde transport of HRP. J Comp Neurol. 1982; 205:63–76. [PubMed: 6121826]

Premkumar A, Marincola F, Taubenberger J, Chow C, Venzon D, Schwartzentruber D. Metastatic melanoma: correlation of MRI characteristics and histopathology. J Magn Reson Imaging. 1996; 6:190–194. [PubMed: 8851427]

Rochat L, Billieux J, Juillerat Van der Linden AC, Annoni JM, Zekry D, Gold G, Van der Linden M. A multidimensional approach to impulsivity changes in mild Alzheimer's disease and control participants: cognitive correlates. Cortex. 2013; 49(1):90–100. [PubMed: 21943808]

Salmon DP. Neuropsychological features of mild cognitive impairment and preclinical Alzheimer's disease. Curr Top Behav Neurosci. 2012; 10:187–212. [PubMed: 22042707]

Sasaki M, Shibata E, Tohyama K, Takahashi J, Otsuka K, Tsuchiya K, Takahashi S, Ehara S, Terayama Y, Sakai A. Neuromelanin magnetic resonance imaging of locus ceruleus and substantia nigra in Parkinson's disease. Neuroreport. 2006; 17:1215–1218. [PubMed: 16837857]

Saunders NL, Summers MJ. Longitudinal deficits to attention, executive, and working memory in subtypes of mild cognitive impairment. Neuropsychology. 2011; 25(2):237–248. [PubMed: 21381828]

Shepherd TM, Thelwall PE, Stanisz GJ, Blackband SJ. Aldehyde fixative solutions alter the water relaxation and diffusion properties of nervous tissue. Magn Reson Med. 2009; 62:26–34. [PubMed: 19353660]

Shibata E, Sasaki M, Tohyama K, Kanbara Y, Otsuka K, Ehara S, Sakai A. Age-related changes in locus ceruleus on neuromelanin magnetic resonance imaging at 3 Tesla. Magn Reson Med Sci. 2006; 5:197–200. [PubMed: 17332710]

Smith BR, Johnson GA, Groman EV, Linney E. Magnetic resonance microscopy of mouse embryos. Proc Natl Acad Sci U S A. 1994; 91:3530–3533. [PubMed: 8170941]

Takahashi, J.; Shibata, T.; Sasaki, M.; Kudo, M.; Yanezawa, H.; Obara, S.; Kudo, K.; Ito, K.; Yamashita, F.; Terayama, Y. Detection of changes in the locus coeruleus in patients with mild cognitive impairment and Alzheimer's disease: high-resolution fast spin-echo T1-weighted imaging. Geriatr Gerontol Int. 2015. http://dx.doi.org/10.1111/ggi.12280. (in press)

Tovi M, Ericsson A. Measurements of T1 and T2 over time in formalin-fixed human whole-brain specimens. Acta Radiol. 1992; 33:400–404. [PubMed: 1389643]

Vazey EM, Aston-Jones G. The emerging role of norepinephrine in cognitive dysfunctions of Parkinson's disease. Front Behav Neurosci. 2012; 6:48. [PubMed: 22848194]

Vazey EM, Aston-Jones G. Designer receptor manipulations reveal a role of the locus coeruleus noradrenergic system in isoflurane general anesthesia. Proc Natl Acad Sci U S A. 2014; 111(10): 3859–3864. [PubMed: 24567395]

Wilson RS, Nag S, Boyle PA, Hizel LP, Yu L, Buchman AS, Schneider JA, Bennett DA. Neural reserve, neuronal density in the locus ceruleus, and cognitive decline. Neurology. 2013; 80(13): 1202–1208. [PubMed: 23486878]

Zarow C, Lyness S, Mortimer J, Chui HC. Neuronal loss is greater in the locus coeruleus than nucleus basalis and substantia nigra in Alzheimer and Parkinson diseases. Arch Neurol. 2003; 60:337–341. [PubMed: 12633144]

Zecca L, Stroppolo A, Gatti A, Tampellini D, Toscani M, Gallorini M, Giaveri G, Arosio P, Santambrogio P, Fariello RG, Karatekin E, Kleinman MH, Turro N, Hornykiewicz O, Zucca F. The role of iron and copper molecules in the neuronal vulnerability of locus coeruleus and substantia nigra during aging. Proc Natl Acad Sci U S A. 2004; 101:9843–9848. [PubMed: 15210960]

Zecca LM, Zucca FAP, Albertini AM, Rizzio EP, Fariello RGM. A proposed dual role of neuromelanin in the pathogenesis of Parkinson's disease. Neurology. 2006; 67(7 Suppl 2):S8–S11. [PubMed: 17030740]

Zucca F, Bellei C, Giannelli S, Terreni MR, Gallorini M, Rizzio E, Pezzoli G, Albertini A, Zecca L. Neuromelanin and iron in human locus coeruleus and substantia nigra during aging: consequences for neuronal vulnerability. J Neural Transm. 2006; 113:757–767. [PubMed: 16755380]

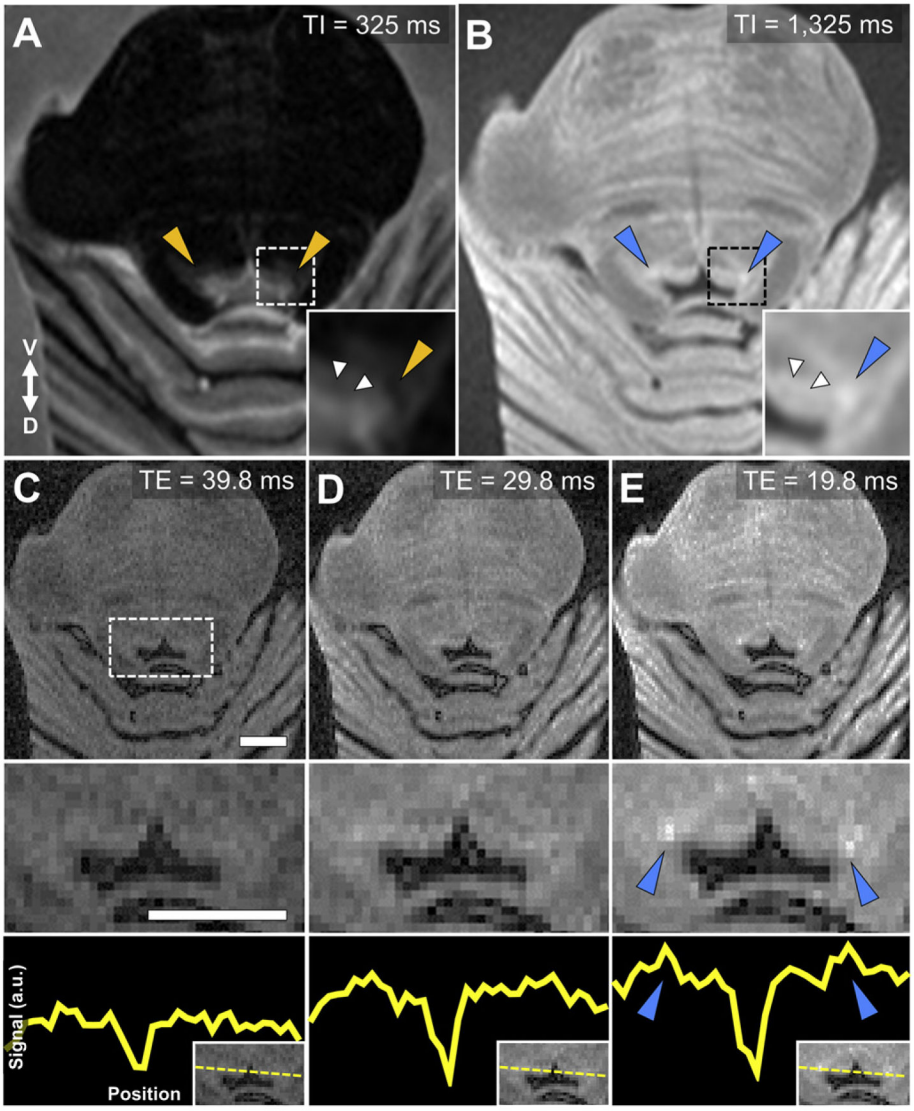

Fig. 1.

Optimal parameters for ex-vivo LC-MRI. A rapid acquisition with refocused echoes (RARE) sequence was used to obtain axial sections from brainstem tissue embedded in agar. A) A short inversion recovery time (TI) produces distinct periaqueductal gray (PAG) contrast compared to surrounding tissue, but no elevated contrast in putative LC regions (orange triangles). B) Elevated contrast is still observed in the PAG with a long TI, as well as specific increased contrast in putative LC regions (blue triangles). C–E) A short echo time (TE) resulted in diminished PAG contrast relative to increased contrast in LC (blue triangles). Magnified 4th ventricular area (dashed box) is presented in the middle row. Bottom row demonstrates the relative increase in LC-MRI contrast with shorter TE using a linear ROI that was used to collect contrast values across the brainstem for each TE acquisition (y-axis: arbitrary units). An axial slice from the same tissue sample (HB 24) is presented in all images (ROI positioning shown in the inset at bottom right). Image parameters common across scans: number of slices = 8, slice thickness = 2 mm, slice

spacing = 0.5 mm, repetition time = 3000 msec, inversion time = 825 ms, number of averages = 3, imaging resonance frequency = 300 MHz, echo train length = 2, flip angle = 180°, matrix size = 128 × 128, field of view = 4.00 × 4.00 cm, in-plane voxel size = 310 μm. Scale bars = 5 mm.

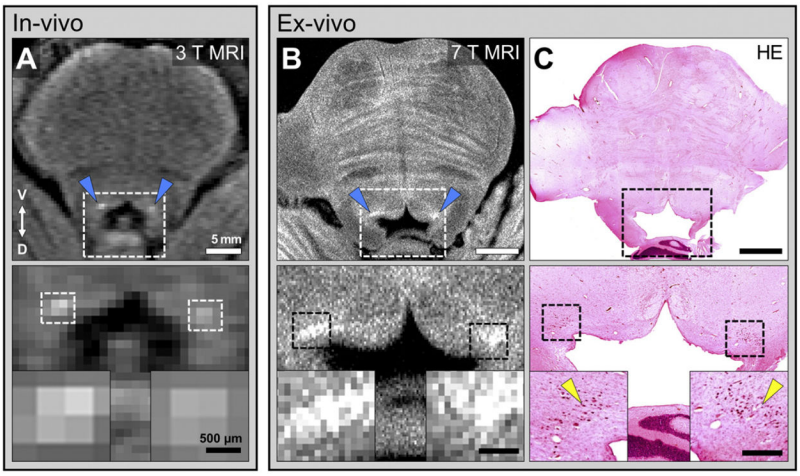

Fig. 2.

MRI microscopy of the human LC (HB24). A long (3 h 11 min) scan acquisition was used to obtain microscopy resolution images (panel B) from post-mortem tissue to allow comparative analysis with histology in the same tissue (panel C). To emphasize the benefit of ultra-high resolution imaging for this project, a typical 3 T T1-TSE 11 min scan of the LC is presented for comparison (panel A). A) Axial slice through the human brainstem obtained using a T1-TSE sequence as described in Keren et al. (2009). Increased contrast can be observed in the putative location of the LC (blue arrows). Double arrow indicates ventral (V) and dorsal (D) directions. A magnified view of the 4th ventricle region (dashed box) is displayed in the bottom panel, with additional detail of the observed contrast (inserts). The spatial extent of putative LC-MRI contrast (dashed box in higher power image below) includes only a few voxels due to relatively limited spatial resolution (400 um in plane resolution). B) Microscopy resolution RARE-INV scan obtained at 7 T MRI with postmortem tissue. Elevated contrast is observed in the putative LC region (blue arrows). Lower panels in A and B show magnified regions indicated by dashed boxes in upper panels. Dashed boxes in lower, high power images indicate location of LC-MRI contrast. C) A bright-field photomicrograph of a hematoxylin and eosin (H&E)-stained 40 µm-thick axial section from the same tissue and equivalent rostral–caudal position as the MRI slice displayed in panel B. Magnification of the ventricle and putative LC regions (bottom panels) demonstrates spatial correspondence between microscopy LC-MRI contrast and H&E-stained neurons in the LC region (yellow arrows; compare panels B and C). Scale bars = 5 mm (top panels), and 500 µm (bottom panel inserts).

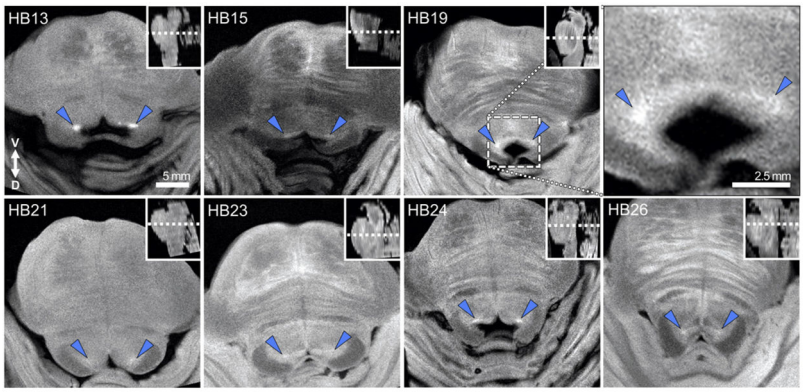

Fig. 3.

7 T MR microscopy (in-plane resolution = 78 μm) through the mid-pons of postmortem brainstem tissue samples across individual cases. For each specimen, an axial section is presented at the level of apparent maximal LC-MRI contrast. The rostral–caudal location of each slice is presented on a mid-sagittal view of the brainstem sample (inserts). Between-sample variation in the putative LC-MRI contrast (blue triangles) can be observed, including focal (e.g. specimen HB13) and diffuse patterns (e.g. specimen HB21) of contrast. The 4th ventricle region of sample HB19 is magnified (top right panel) to demonstrate anatomical detail, varied tissue contrasts, and detailed LC morphology that can be observed utilizing the ex-vivo microscopy-resolution RARE-INV acquisition.

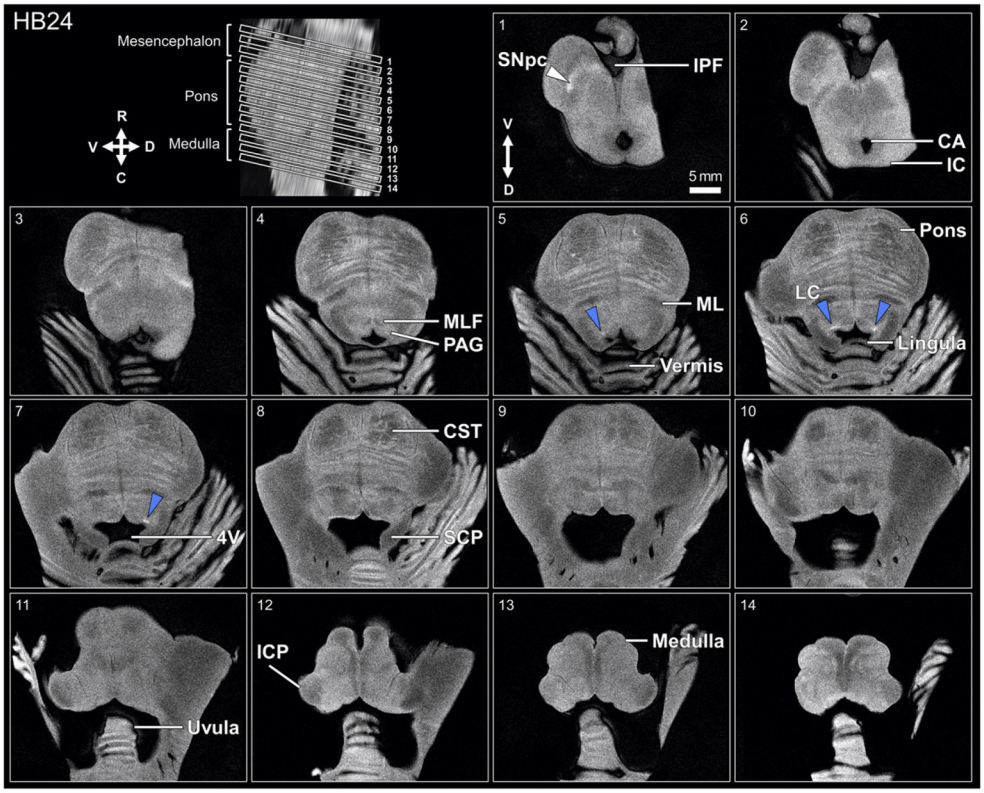

Fig. 4.

Axial slices of an ex-vivo brainstem sample (HB24) obtained with 7 T MRI using RARE-INVersion recovery sequence. Slices in panels numbered 1–14 correspond to slices taken through the brainstem in upper left panel. Elevated contrast is observed in regions corresponding to the left substantia nigra, pars compacta (SNpc, white triangle, panel 1), and the locus coeruleus (LC, blue triangles, panels 5–7). Within-specimen morphological asymmetry in putative LC-MRI contrast can be observed for slices 5–7. Anatomical landmarks are indicated to facilitate orientation: 4th ventricle (4 V), cerebral aqueduct (CA), corticospinal tract (CST), inferior cerebellar peduncle (ICP), inferior colliculus (IC), interpeduncular fossa (IPF), medial lemniscus (ML), medial longitudinal fasciculus (MLF), periaqueductal gray (PAG), superior cerebellar peduncle (SCP). Arrows indicates ventral (V), dorsal (D), rostral (R), and caudal (C) directions.

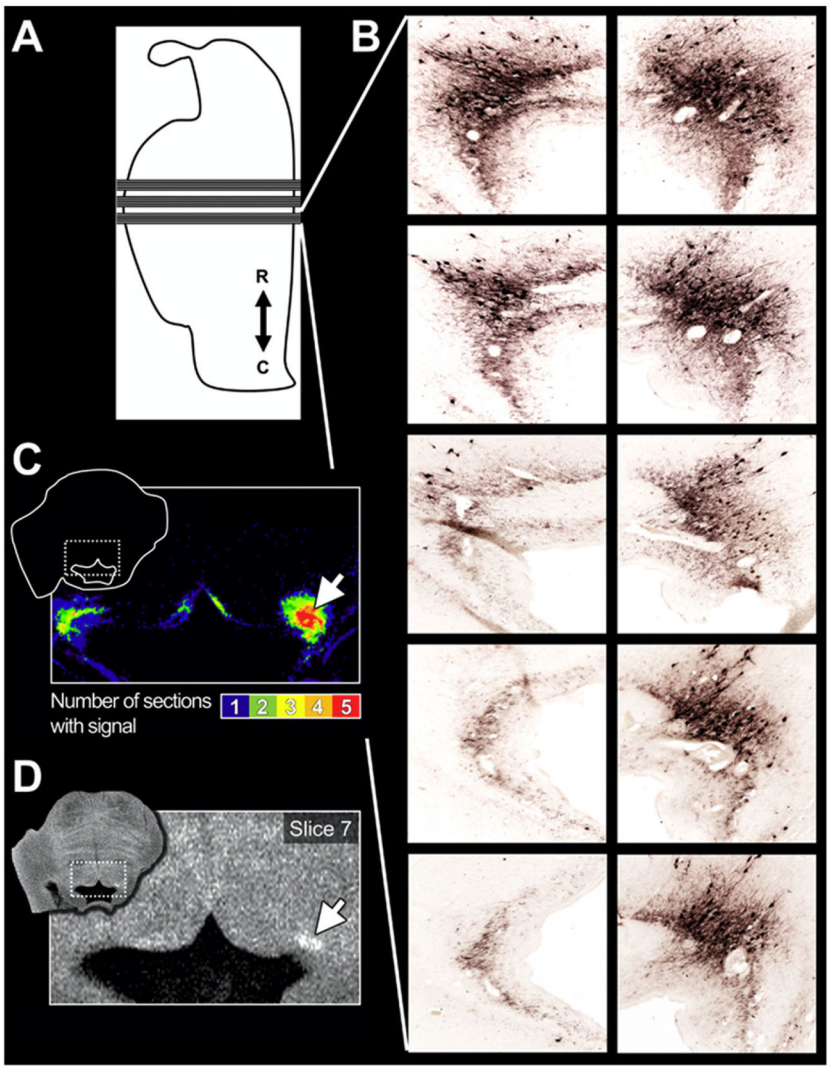

Fig. 5.

LC-MRI contrast depends on the consistency of TH+ LC neurons across the thickness of an MRI slice. A) Illustration of a mid-sagittal section through the HB24 brainstem. Lower rectangles and lines extending from the illustration to indicate the histological sections shown in (B). B) TH+ neurons from the left and right LC (left and right column of images) for the 5 equidistant 40 μm-thick section images that span the thickness of the MRI slice. Note the limited TH staining in LC processes (left) in comparison to dense staining for clusters of LC cell bodies on the right. C) The density of staining for the left and right LC was represented by binarizing the TH images and summing to create a TH density map that also demonstrates the greater density of TH+ LC neurons on the right. This also coincides with the more pronounced LC-MRI contrast on the right in (D). Slice 7 can also be seen in Figs. 4 and 6.

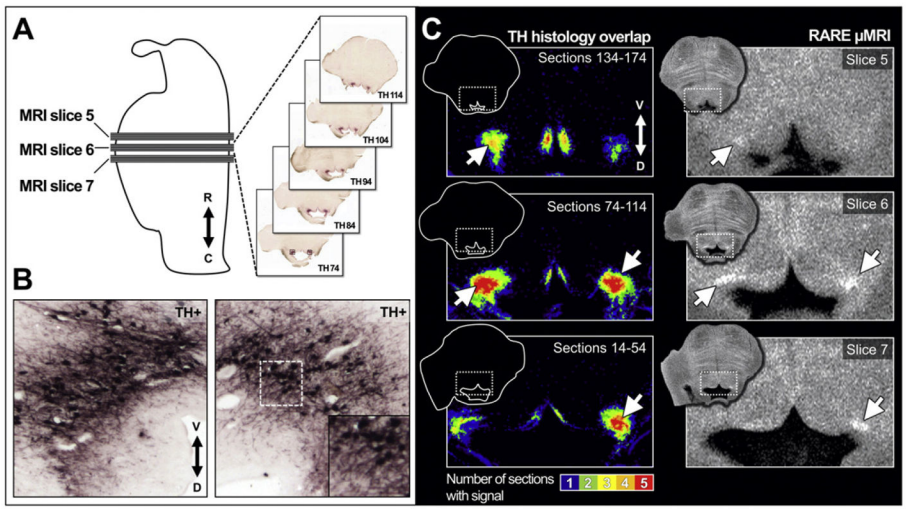

Fig. 6.

TH+ LC neuron density spatially corresponds to increased RARE-INVersion recovery contrast. The same tissue sample as in Fig. 4 (HB24) underwent MRI scanning and was then sectioned for histological analysis. A) Illustration of a mid-sagittal section through the brainstem. Gray rectangles (MRI slices 5–7) represent the position of three 2-mm-thick consecutive RARE-INV (µMRI) axial sections (see Fig. 4, panels 5–7) in which putative LC-MRI contrast can be observed. The five consecutive, equidistant 40 µm-thick sections (black lines) contained within each of the three MRI slices (indicated at right in panel A) were immunohistochemically stained for TH to visualize NE neurons in LC. Double arrow indicates rostral (R) and caudal (C) directions. B) Magnified view of left and right TH-stained neurons and processes in LC. Both photomicrographs are from histology section TH 74, the most caudal of five sections comprising MRI slice 6 in panel A. Double arrow indicates ventral (V) and dorsal (D) directions. C) LC TH+ density maps and corresponding LC-MRI contrast. In each row a TH+ signal density map (left) is shown next to its corresponding MRI slice (right). The histology sections (panel A) were processed and spatially rigidly aligned to a common stable anatomical landmark to produce TH density maps (see Methods). Note that LC-MRI contrast is most pronounced for slices (white arrows in panels at right) in which TH staining was observed across all 5 sections for that MRI slice (red: TH staining on all 5 sections; blue: TH staining on 1 section).

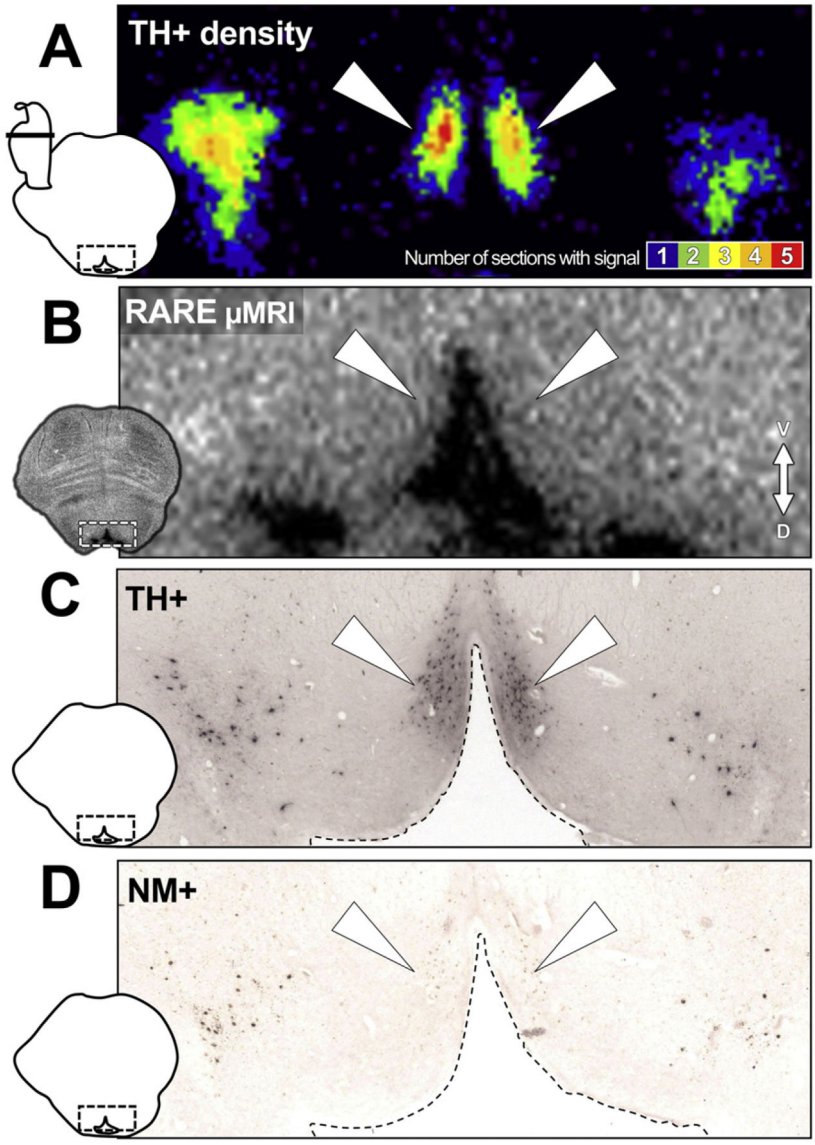

Fig. 7.

TH+ neurons that produce neuromelanin are necessary for LC-MRI contrast. Increased TH+ density in HB24 did not always spatially correspond to increased MRI signal. A) TH+ density map of the 4th ventricle region in the rostral pons (from sections through MRI slice 5 in Figs. 4 and 6C). In addition to the LC TH signal on either side, increased TH+ density can be observed in midline regions flanking the ventral border of the 4th ventricle (white triangles), corresponding to the location of the caudal dorsal raphe nucleus (dRN). B) RARE-INV microscopy (μMRI) of the same tissue as in A. No increase in contrast was observed in the periventricular area corresponding to dRN TH+ signal (white triangles). C) Bright field photomicrograph of the 4th ventricle region at the rostral pons in a 40 μm-thick section stained for TH. The section presented is from the same tissue and from within the slab imaged in (B). As expected, TH+ cells and proximal neurites can be observed (white triangles) in the same region as increased TH+ density in (A), corresponding to the dRN. D)

Bright field photomicrograph of the same region in an unstained section, showing neuromelanin (NM+) granule distribution. Although neuromelanin granules can be observed in the same area as the TH+ neurons of the LC (C) near the left and right boundaries of the image, they are absent from the more medial dRN area (white triangles).

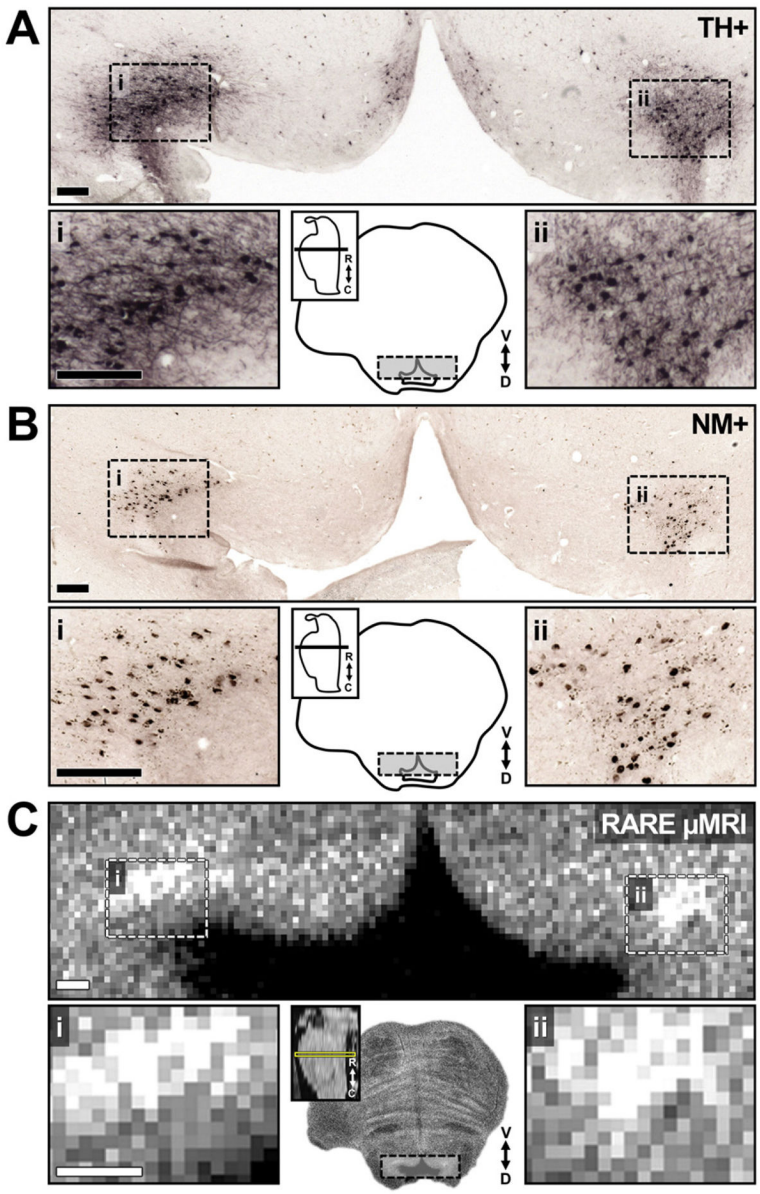

Fig. 8.

Increased RARE-INV contrast corresponds to the location of TH+ neuromelanin containing neurons of the LC. Photomicrographs and MRI microscopy acquisition from HB24. A) TH-stained tissue showing NE neurons in LC. Magnified panels of left and right LC (lower) show the extent of NE cell bodies and proximal neurites. B) Unstained section showing distribution of neuromelanin (NM) granules in the same tissue section as A. Magnified panels (lower) display depositions of large intracellular granules as well as smaller extracellular neuromelanin in LC. C) RARE-INV (μMRI) scan of the same region with microscopy resolution. Magnified panels in A, B and C demonstrate correspondence of increased MRI contrast with distribution of NM granules in LC, and overlapping with the location of NE cells in LC.

Table 1

Demographics, neuropathology and tissue fixation information for $N = 7$ brain donors.

	Donor characteristics					Tissue fixation		
	Demographics		CNS diagnosis			Processing intervals (hrs)		
Sample ID	Age (years)	Sex	Race	Clinical	Histopathology	PMI [a]	Time to fixation	Fixation
HB13	79	Male	Caucasian	AD [b]	ATD [c]	3.0	1.0	96.0
HB15	67	Female	Caucasian	AD	ATD	18.0	5.0	96.0
HB19	76	Male	Caucasian	AD	AD	6.5	1.0	144.0
HB21	81	Female	Caucasian	AD	ATD	6.0	5.0	96.0
HB23	79	Male	Caucasian	AD	ATD	6.0	1.0	96.0
HB24	91	Female	Caucasian	AD	AD NFTP [d]	3.5	1.0	96.0
HB26	62	Female	Caucasian	AD	LBD [e]	20.8	1.0	96.0

[a] PMI — Post-mortem interval.

[b] AD — Alzheimer's disease.

[c] ATD — Alzheimer type dementia.

[d] AD NFTP — Alzheimer's disease, neurofibrillary tangle-predominant.

[e] LBD — Lewy body dementia.